Scientific Research Publishing

Open Journal of Geology, 2025, 15(8), 425-454
https://www.scirp.org/journal/ojg
ISSN Online: 2161-7589
ISSN Print: 2161-7570

Mixed-Source Post-Collisional Magmatism in the Rhodope Metamorphic Complex: New Geochemical and Isotopic Insights from the Elatia Pluton (N. Greece)

Kyriaki Pipera

Department of Mineralogy, Petrology, Economic Geology, School of Geology, Aristotle University of Thessaloniki, Thessaloniki, Greece
Email: piperakyr@gmail.com

How to cite this paper: Pipera, K. (2025) Mixed-Source Post-Collisional Magmatism in the Rhodope Metamorphic Complex: New Geochemical and Isotopic Insights from the Elatia Pluton (N. Greece). *Open Journal of Geology*, **15**, 425-454.
https://doi.org/10.4236/ojg.2025.158021

Received: July 10, 2025
Accepted: August 19, 2025
Published: August 22, 2025

Abstract

Tertiary to Early Miocene post-collision granitoids intrude the whole Rhodope Metamorphic Complex (RMC; northern Greece and southern Bulgaria) during the extensional event that followed the collapse of the orogen. The Barutin-Buynovo-Elatia-Skaloti-Paranesti batholith in northern Greece and southern Bulgaria is the largest plutonic body of the Rhodope Metamorphic Complex (RMC) and is rather significant among these numerous post-collision plutons. A new field survey, combined with new whole-rock major, trace, REE, and Sr-Nd isotope analyses, focuses on the Elatia granodiorite in northern Greece and its mafic enclaves and diorite for the first time by representing members that record the earliest stages of magma evolution. All rocks display typical subduction-related characteristics with enrichment in LILE and LREE and depletion in HFSE but with enrichment in MREE. Major and compatible trace elements decrease smoothly with increasing SiO_2 from the enclaves to the most evolved granodiorite, consistent with fractional crystallization of hornblende, biotite, plagioclase, titanite, and apatite. The alkaline enclaves and diorite, together with the "adakitic" character of the granodiorite, suggest high degrees of melting of a volumetrically minor mantle component. The diorite has a very low $^{87}Sr/^{86}Sr$ ratio (0.70425) and high $^{143}Nd/^{144}Nd$ (0.51269), the lowest and highest values respectively among the Eocene plutons so far in RMC, pointing to an origin from a depleted mantle melt. Isotope ratios for the granodiorite and enclaves lie between the depleted mantle and the RMC crust, implying intense magma mixing. Probability-based discrimination diagrams place the pluton in the post-collision field. All data indicate an early post-collisional origin at ~56 Ma, rather than pre-collision. Mafic-felsic mixing members with

concurrent FC (fractional crystallization) provide the best explanation for the spread of the geochemical indicators. These results realign the Elatia pluton with other early Eocene, post-collisional granites of the RMC, providing a framework for future research.

Keywords

Magmatic Enclaves, Elatia Pluton, Rhodope Metamorphic Complex, Eocene Magmatism

1. Introduction

The Elatia pluton lies north of the city of Drama. It forms the central part of the Elatia-Skaloti-Paranesti complex, which, together with the Barutin-Buynovo pluton in SW Bulgaria, makes up the largest batholith of the Rhodope Metamorphic Complex (RMC) [1]-[5]. The pluton intrudes the metamorphic rocks of the Middle Allochthon or Sidironero Unit [6] of the Hellenic RMC, displaying only limited contact metamorphism effects. It comprises four main rock types (**Figure 1**):

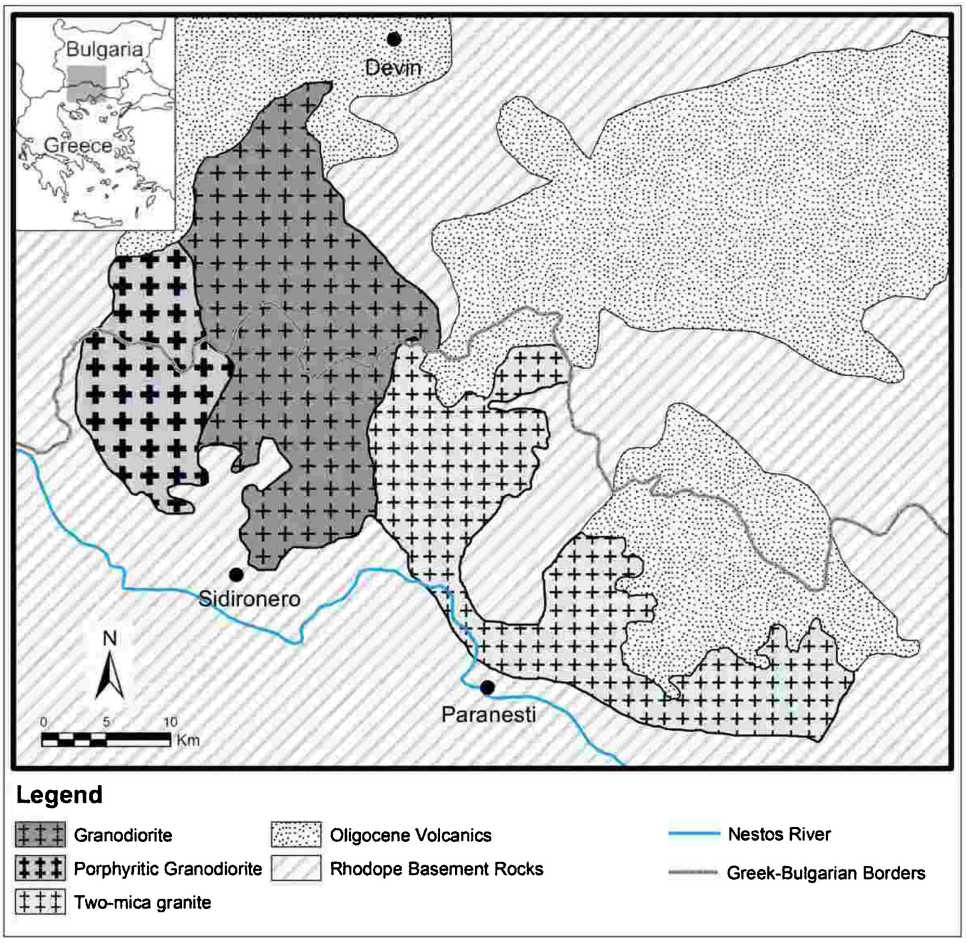

Figure 1. Simplified map of the Elatia pluton. Modified after Soldatos *et al.* [18].

1) a (hornblende)-biotite granodiorite in the center, which becomes porphyritic towards the northern and central-west margins and locally grades into quartz-diorite or monzogranite; 2) a two-mica granite to leucogranite that intrudes the granodiorite in the east; 3) a biotite granite to leucogranite that cuts the granodiorite across the whole outcrop as non-mappable dykes that vary in thickness from several centimeters to several meters [3]-[5]. Scarce enclaves of several centimeters to decimeters in size occur in the granodiorite, but no geochemical data have yet been published.

In this study, we present new petrological and geochemical data for the granodiorite of the Elatia pluton, most notably the first Nd-isotope analyses ever reported for this body, along with the first detailed analyses of its mafic enclaves and diorite. These mafic members are key evidence that can help close the gap in unraveling the origin and evolution of the plutonic body, thereby providing essential insight into the area's geotectonic evolution. These new results, combined with existing geochemical constraints, allow us to re-evaluate the petrogenesis and magmatic evolution of the Elatia pluton and define a more narrowly defined geotectonic framework for the region.

2. Geological Background

The RMC occupies a large area between the internal part of the Hellenides orogen, between the Vardar suture to the west and the Maritsa fault zone to the north, occupying southern Bulgaria and northern Greece. It is defined as a key area for understanding the evolution of the Tethyan systems. It is formed from Mesozoic synmetamorphic south-vergent nappes [6] of high-grade metamorphic and igneous rocks (e.g., [7]-[9]). These nappes are stacked in an Alpine active margin environment, formed during the closure of the Tethys Ocean [10]. Synmetamorphic compression versus syn- to post-orogenic extension and progressive exhumation of deep crustal levels characterize the Alpine structural evolution of the RMC. Large-scale extension has affected the area since the middle Eocene as a response to gravity spreading of the previously formed thick and weak crustal-scale orogenic wedge [11].

The RMC is composed of the Northern Rhodope Domain, the Northern Rhodope Core Complex (NRCC) on the NE, and the Southern Rhodope Core Complex on the SW and N-NW (SRCC; [12]). The NRD is comprised of the imbricate units [2] [13], dominated by an eclogite-metabasite-gneiss and a gneiss-marble sequence [4] [14] [15]. The NRCC is comprised of ortho- and paragneisses, migmatites, schists, amphibolites, and metapelites. The SRCC is dominated by flat-lying units of marbles and orthogneisses, and to a lesser extent, micaschists, paragneisses, and amphibolites, with the core of the SRCC called the Drama window [2], which consists of rocks of the lower terrane. Nappes' stacking took place during alternating periods of continental crust segment collision and oceanic lithosphere subduction. Subsequently, extensional tectonics associated with detachment faults and ductile to brittle tectonics from Paleocene to Early Miocene times

led progressively to orogen collapse and exhumation of deep crustal levels. This extensional period was accompanied by syn- to post-tectonic granitoid intrusions [16]. The Elatia pluton intrudes the imbricate units of Madan-Sidironero eclogites and gneisses and the Asenitsa marble-gneiss unit [1] [2] [12].

According to Jones *et al.* [17], foliation in granodiorite is variably developed, with the strongest foliations near and aligned parallel to the southern lower contact with partially migmatized gneissic basement rocks. At this basal contact, shallow northward-dipping, meter-scale, sheet-like layers reflect the larger structure of the intrusion; the western margin is also foliated [17]. Both layering and foliation run sub-parallel to the penetrative foliation in the bordering country rocks; locally, there are large bodies of country rock at the base of the granite sheets, and the granite and country rock foliations are broadly concordant. Biotitic xenoliths are locally abundant, especially towards the southern part of the intrusion, and several generations of pegmatites and aplites are present [17].

The age of the Elatia pluton was debatable for many years. Biotite K-Ar dating from both the Greek and Bulgarian parts of the batholith ranges from 29.1 ± 1.2 to 45.0 ± 2.0 Ma [3] [17]. Kotopouli [3] reported a possible intrusion age of Upper Cretaceous or Lower Tertiary based on geological data in the Skaloti area. Soldatos *et al.* [18], based on Rb-Sr geochronology, suggest an age older than 48 Ma. The age of the Elatia pluton was finally established with the U-Pb method on granodiorite zircons at about 56 Ma [19].

Soldatos *et al.* [18] argued that the granodiorite (and porphyritic granodiorite), granite, and two-mica granite form three distinct rock groups. A genetic link between granodiorite and granite seems plausible at first glance, based on the major and most of the trace element variation diagrams; however, it is ruled out by the Zr, Ba, Th, and REE patterns, as well as Sr isotopes. A genetic relation between granite and two-mica granite is also ruled out due to the consistent cross-cutting trends, although their REE patterns and Sr isotopes can support a genetic relation.

Soldatos *et al.* [18] argued that the granodiorite (and porphyritic granodiorite), granite, and two-mica granite form three distinct rock groups. A genetic link between granodiorite and granite seems plausible at first glance, based on the major and most of the trace element variation diagrams; however, it is ruled out by the Zr, Ba, Th, and REE patterns, as well as Sr isotopes. A genetic relation between granite and two-mica granite is also ruled out due to the consistent cross-cutting trends, although their REE patterns and Sr isotopes can support a genetic relation.

Several authors have discussed the geotectonic setting of the Elatia pluton. Jones *et al.* [17], using the R1-R2 diagram of Batchelor & Bowden [20], suggested a post-collision uplift tectonic setting for the Greek part of the batholith due to crustal thickening, although their data plot in the anatectic field (syn-orogenic). For the same part of the batholith, Soldatos *et al.* [18], using the same and the Harris *et al.* [21] diagram, suggested that the magma genesis is related to a subduction tectonic environment, most likely prior to the collision.

3. Materials and Methods

For this study, we combined previously published data with new results. The dataset of the latest unpublished result includes three major-element analyses (two enclave samples and one diorite), twenty-six trace element and REE analyses, six Sr-isotope analyses, and nine Nd-isotope analyses. The trace-element, REE, and Nd-isotope analyses were obtained from the exact same samples analyzed by Soldatos *et al.* [18].

Major and some trace-element analyses (Cr, Ni, Sc, V, Pb, Zr, Rb, Ba, Sr, Nb) were performed at Saint Mary's University (Halifax, Canada) on a Philips (Panalytical) PW2400 X-ray spectrometer with the Philips PW2510 102-position sample changer. Major and some trace-element analyses (Cr, Ni, Sc, V, Pb, Zr, Rb, Ba, Sr, Nb) were performed at Saint Mary's University (Halifax, Canada) on a Philips (Panalytical) PW2400 X-ray spectrometer with the Philips PW2510 102-position sample changer. The PW2400 is a wavelength-dispersive sequential spectrometer, which utilizes a 3 kW Rh anode to produce a continuum of primary X-rays used to excite the sample. The fluorescing wavelengths from the sample are separated using natural and synthetic crystals, and the photons are captured by either a flow detector or a scintillation counter. The major elements were measured on fused glass beads. Beads were prepared by mixing 5 g lithium tetraborate, 300 mg lithium fluoride, and 35 mg lithium bromide with 1 g sample and fusing the mixture in a platinum crucible using the Claisse Fluxy at a temperature of approximately 1050˚C. The melts are mounted into 30 mm disks and analysed. Trace elements are determined on pressed pellets. These are prepared by mixing 10 g sample with 1.5 g powdered Bakelite (a phenol-formaldehyde co-polymer) and pressing the mixture into a disk approximately 5 mm thick and 40 mm in diameter using the Herzog press at 20 tonnes for 10 seconds. The pellets are heated to 180˚C for 15 min and cooled to produce a sample for analysis. All data are corrected either using theoretically determined alpha coefficients (e.g., major elements) or by using Compton scatter (e.g., trace elements). Accuracy for this method for silica is within 0.5%. The error is less than 1% for the other major elements. For trace elements, the accuracy is within 5%. Instrument precision, as defined by repeated analysis of a single sample, is within 0.6% relative. Sample precision, as defined by measurement of different samples taken from the same aliquot, is within 1% for elements done on fused beads and 0.7% for those done on pressed pellets.

Some trace elements and REE analysis were performed by a Laser Ablation-Inductively Coupled Plasma-Mass Spectrometer (LA-ICP-MS) system installed at the Earth Sciences Department of Perugia University (belonging to the Scientific Methodologies Applied to Archaeology and Art (SMAArt) Center), composed of a commercial New Wave UP213 (New Wave, UK) LA system coupled with a Thermo Electron X7 (Thermo Electron Corporation, Waltham, USA) ICP-MS. The laser ablation system is a frequency-quintupled Nd:YAG laser, whose fundamental wavelength of 1064 nm is converted into 213 nm by means of three harmonic generators. The commercial ablation cell (New Wave, UK), capable of sup-

porting both thin sections and cylindrical resin chips, has been modified in order to mount both reference materials and unknown samples together. In addition, special adjustments have been developed on the ablation cell for lodging "large" samples (up to c.a. 5 cm). Helium is preferred over argon as a carrier gas to enhance the transport efficiency of the ablated aerosol [22]. The helium carrier gas exiting the ablation cell is mixed with argon make-up gas before entering the ICP torch; this configuration permits the maintenance of stable and optimum excitation conditions. LA-ICP-MS measurements are carried out using time-resolved analysis operating in a peak-jumping mode. The laser repetition rate and the laser energy density are fixed at 10 Hz and ~10 J/cm^2, respectively. The LA-ICP-MS system is optimized for dry plasma conditions prior to each analytical session on a continuous linear ablation of the NIST SRM 612 glass standard by maximizing the signals for selected masses (La+ and Th+) and reducing oxide formation by minimizing the ThO+/Th+ ratio. Data are collected in discrete runs of 15 - 24 analyses, each run comprising 6 - 15 unknowns and 1 quality control standard analyzed as an unknown, bracketed by 8 analyses of the external standard. External calibration is performed using NIST SRM 610 and 612 glass standards in conjunction with internal standardization using a major element, generally 29Si or 42Ca (Fryer *et al.*, 1995), previously determined by an independent technique (e.g. EPMA or XRF) following the proposed method [23]. Unknown samples are mounted together with standards in order to avoid changes in instrumental conditions due to the continuous opening of the ablation cell interface. A typical analysis consists of acquiring 60 s of background followed by 60 s of the signal produced by the ablated aerosol. Data reduction is performed on the time-resolved signals by carefully selecting a homogeneous portion of background and signal intensity. Data reduction is performed using the Glitter software [24] and in-house written codes.

The Sr and Nd isotope analytical work was performed at the Laboratory of Geochronology, Department of Lithospheric Research, University of Vienna. Results are based on the TIMS procedure. The Sr and Nd isotope analytical work was performed at the Laboratory of Geochronology, Department of Lithospheric Research, University of Vienna. Results are based on the TIMS procedure. Powders of selected samples (c. 100 - 200 mg) were digested in tightly screwed Savillex beakers using an ultrapure mixture of HF:$HClO_4$ (5:1) for 2 weeks at 100˚C - 110˚C on a hot plate. After acid evaporation, repeated treatment of the residue using 5.8 N HCl resulted in clear solutions. Element extraction (Sr, REE) was performed using AG 50W-X8 (200 - 400 mesh, Bio-Rad) resin and 2.5 N and 4.0 N HCl as eluants. Nd was separated from the REE group using Teflon-coated HdEHP and 0.18 N HCl as eluant. Maximum total procedural blanks were <1 ng for Sr and 50 pg for Nd, and were considered negligible. The pure element fractions were evaporated using a Re double filament assembly and run in static mode on a Thermo-Finnigan Triton TI TIMS machine. A mean 87Sr/86Sr ratio of 0.710268 ± 0.000006 (n = 4) was determined for the NBS987 (Sr) and a mean $^{143}Nd/^{144}Nd$

ratio of 0.511844 ± 0.000003 (n = 4) for the La Jolla (Nd) international standards during the period of investigation. Within-run mass fractionation was corrected for 88Sr/86Sr = 8.3752, and $^{146}Nd/^{144}Nd$ = 0.7219, respectively. Errors quoted represent 2s errors of the mean. For Nd, a continuous depletion of the upper mantle is assumed throughout geological time, and the following Depleted Mantle (DM) model parameters were used: $^{147}Sm/^{144}Nd$ = 0.222, $^{143}Nd/^{144}Nd$ = 0.513114 [25].

Data processing was carried out using the Geochemical Data Toolkit (GCDKit) [26] and Petrograph [27].

4. Results

4.1. Major and Trace Elements and Sr, Nd Isotope Analysis

Table 1 & Table 2 summarize the analytical results from this study, combined with analyses reported by previous authors [17] [18].

Table 1. Analysis results of the major and trace elements integrated with published analyses from earlier studies.

Sample	PEL-1	PEL-3	PEL-4	A-06	A-10	A-23	D-05	D-08B	D-11A	DSK-09	DSK-14
Type	Enclave	Enclave	Diorite				Granodiorite				
Reference*	1	1	1	3	3	3	3	3	3	3	3
SiO_2	51.24	52.02	51.46	62.57	64.89	65.78	61.32	63.81	65.38	64.31	69.68
TiO_2	1.27	1.13	0.83	0.69	0.61	0.53	0.68	0.63	0.54	0.60	0.43
Al_2O_3	19.17	18.14	20.28	17.60	17.08	16.69	17.57	16.87	16.60	16.89	15.33
FeOtot	6.57	7.43	6.96	4.00	3.03	3.02	4.21	3.45	3.08	3.37	2.23
MnO	0.12	0.14	0.18	0.08	0.06	0.06	0.09	0.09	0.09	0.09	0.08
MgO	4.23	4.61	3.07	2.35	1.61	1.69	1.99	1.66	1.54	1.57	0.99
CaO	6.17	5.92	7.36	4.89	3.77	3.92	5.17	4.35	3.62	4.01	2.70
Na_2O	4.49	4.09	4.01	3.99	4.09	4.07	4.20	4.15	4.06	3.92	4.12
K_2O	2.83	3.02	3.04	2.06	2.54	2.52	2.23	2.81	3.18	3.09	2.77
P_2O_5	0.54	0.54	0.53	0.37	0.33	0.30	0.41	0.36	0.28	0.34	0.20
Mg#	53.4	52.5	44.0	51.1	48.6	49.9	45.7	46.1	47.1	45.4	44.1
LOI	2.2	1.8	1.9	1.2	1.8	1.2	1.8	1.6	1.4	1.6	1.3
Sum	98.8	98.8	99.6	99.8	99.8	99.7	99.7	99.8	99.7	99.7	99.9
XRF											
Sc	15	16		9	6	8	11	13	8	7	6
V	162	169		65	61	50	84	67	53	61	42
Cr	1	37		36	31	30	36	32	29	29	25
Ni	15	45		18	13	9	18	14	15	12	6
Pb	8	11		10	15	10	9	14	15	14	17

Continued

Zr	285	274		284	216	217	296	246	243	253	193
Nb	26	16		25	13	20	11	22	18	17	15
U	2	2		4	5	5	1	2	4	8	6
Y	26	17		22	14	15	11	15	15	15	16
Th	18	11		16	19	14	18	15	13	17	18
Rb	106	148		86	178	88	100	107	114	102	114
Sr	871	677		715	376	589	835	658	613	732	422
Ba	663	609		635	596	564	659	788	909	921	316
ICP-MS											
Sc			10.9								
V	167.0	171.0	208.4								
Cr	1.1	36.8	18.5								
Ni	11.7	37.0									
Pb			17.8								
Zr			78.1								
Hf	6.3	6.7	1.9				5.6				
Nb	24.1	14.0	4.8								
Ta	1.20	0.70	0.46				0.60				
U	3.0	2.0	2.3				2.4				
Y	26.3	16.6	21.6				16.0			17.0	
Th	19.3	15.5	6.8				24.5				
Rb	109.4	152.6	98.6				93.0				
Cs	2.5	10.1	3.3				6.1				
Sr	857.7	674.9	1173.5								
Ba	696.0	600.0	728.4				640.0				
La	59.00	48.90	23.29				78.85			61.18	
Ce	120.60	94.40	52.95				135.94			107.69	
Pr	12.46	9.34	6.23				12.16			10.55	
Nd	46.00	33.10	29.62				44.19			40.35	
Sm	7.62	5.24	6.27				5.13			5.69	
Eu	1.72	1.03	1.50				1.19			1.24	
Gd	6.33	4.02	5.78				3.59			4.35	
Tb	0.91	0.60	0.71								
Dy	4.93	3.15	4.05				2.66			3.33	
Ho	0.91	0.59	0.83				0.58			0.69	

Continued

Er	2.58	1.67	2.22	1.76	1.80
Tm	0.37	0.23	0.38		
Yb	2.35	1.47	2.05	1.28	1.34
Lu	0.34	0.22	0.24	0.21	0.20
ΣREE	266.1	204.0	136.1		
Eu/Eu*	0.7	0.7	0.7	0.8	0.7
(La/Lu)cn	18.0	23.1	9.9	39.0	31.8
(La/Sm)cn	4.9	5.9	2.3	9.7	6.8
(Gd/Yb)cn	2.2	2.2	2.3	2.3	2.6
(Tb/Lu)cn	1.8	1.9	2.0		

*1. Major and trace elements from the present study; 2. Major elements, Soldatos *et al.* [18] and trace elements from the present study; 3. Major and trace elements from Soldatos *et al.* [18]; 4. Major and trace elements from Jones *et al.* [17].

Sample	DSK-15	DSK-17	DSK-18	E-04	E-06	E-07	E-09	E-10	GBT.189	GBT.191	GBT.192
Type	Granodiorite										
Reference*	3	2	3	2	3	3	3	3	4	4	4
SiO_2	67.72	59.84	64.87	60.13	73.56	61.37	69.99	66.45	71.60	62.90	67.40
TiO_2	0.50	0.76	0.56	0.73	0.00	0.77	0.39	0.57	0.31	0.72	0.62
Al_2O_3	15.87	17.72	16.72	18.50	15.50	18.19	15.77	16.03	14.80	16.80	16.80
FeOtot	2.48	4.86	3.32	4.41	0.62	4.04	2.19	3.16	1.80	3.87	3.33
MnO	0.08	0.15	0.09	0.09	0.11	0.08	0.08	0.09	0.00	0.09	0.12
MgO	1.11	2.41	1.65	2.29	0.07	2.06	1.11	1.39	0.50	1.70	1.40
CaO	2.84	5.28	4.26	5.14	0.29	4.39	3.20	3.98	2.30	4.10	3.50
Na_2O	3.85	4.29	4.03	4.67	4.89	4.16	4.35	4.13	4.00	3.80	5.10
K_2O	3.60	1.89	2.68	2.67	4.38	2.44	1.80	2.52	4.02	2.83	2.40
P_2O_5	0.22	0.44	0.33	0.44	0.05	0.35	0.13	0.30	0.10	0.27	0.22
Mg#	44.4	46.9	47.0	48.0	16.7	47.6	47.4	43.9	33.1	43.9	42.8
LOI	1.5	2.0	1.2	0.8	0.7	2.1	0.9	1.1	-	-	-
Sum	99.8	99.6	99.7	99.8	100.1	100.0	99.9	99.8	99.4	97.1	100.9
XRF											
Sc	7	12	11	10	1	9	9	12			
V	48		61	78	7	68	37	54	28	84	65
Cr	29	32	34	28	21	28	24	28	7	14	11
Ni	10	21	12	10	0	4	3	10	0	6	2
Pb	20	9	9	10	21	11	22	18			
Zr	203	285	242	344	56	300	223	234	184	213	180

Continued

Nb	19	18	11	25	27	24	14	19	5	21	28
U	5	3	3	4	9	2	1	4	6	6	5
Y	16	22	15	19	8	17	8	18	7	23	22
Th	14	14	12	15	5	17	4	14	19	20	20
Rb	135	117	128	112	337	83	90	101	143	119	170
Sr	476	791	689	821	49	758	433	556	304	538	475
Ba	722	414	1186	728	83	910	235	501	803	535	497
ICP-MS	67.72										
Sc	0.50										
V	15.87	88.0									
Cr	2.48										
Ni	0.08										
Pb	1.11										
Zr	2.84	239.8		292.1							
Hf	3.85	5.6	4.5	7.0					5.1	5.7	5.0
Nb	3.60	16.3		17.5							
Ta	0.22	1.50	1.10	1.20					0.20	1.28	1.99
U	44.4	3.2	1.6	4.6							
Y	1.5	18.1	17.0	15.1							
Th	99.8	18.4	17.2	18.0							
Rb		85.7		105.5							
Cs	7	3.5	3.5	4.1							
Sr	48	762.0		817.7							
Ba	29	511.0		737.0							
La		60.70	47.17	70.50							
Ce		108.30	85.64	123.20							
Pr		10.80	8.74	11.86				8.68			
Nd		37.20	33.57	39.40							
Sm		5.64	4.91	5.85				4.82	4.39	6.60	5.90
Eu		1.27	1.09	1.33				1.07	0.71	1.37	1.01
Gd		4.76	3.73	4.79				3.78			
Tb		0.65		0.62					0.31	0.69	0.63
Dy		3.25	3.04	3.16				3.15			
Ho		0.58	0.67	0.60				0.81			
Er		1.68	1.70	1.62				1.83			

Continued

Tm	0.24		0.24					
Yb	1.54	1.35	1.50	1.58	0.53	1.71	1.47	
Lu	0.23	0.19	0.23	0.23	0.08	0.28	0.25	
ΣREE	236.8		264.9	184.6			169.8	
Eu/Eu*	0.7	0.7	0.7	0.7			0.9	
(La/Lu)cn	27.4	25.8	31.8	19.9	50.6	18.4	18.9	
(La/Sm)cn	6.8	6.0	7.6	5.8	5.6	4.7	4.9	
(Gd/Yb)cn	2.5	2.2	2.6	1.9				
(Tb/Lu)cn	1.9	0.0	1.8		2.6	1.7	1.7	

*1. Major and trace elements from the present study; 2. Major elements, Soldatos *et al.* [18], and trace elements from the present study; 3. Major and trace elements from Soldatos *et al.* [18]; 4. Major and trace elements from Jones *et al.* [17].

Sample	GBT.194	I-11B	I-14A	I-16	M-10	PEL-3H	PS-01	PS-11	PS-12	PS-3	Z-12B
Type	Granodiorite										
Reference*	4	3	2	3	3	2	2	2	3	3	3
SiO_2	67.80	66.09	70.24	63.24	69.18	60.52	66.92	65.88	65.94	70.50	66.78
TiO_2	0.62	0.52	0.37	0.64	0.43	0.75	0.61	0.54	0.55	0.36	0.53
Al_2O_3	16.60	16.66	15.36	16.98	15.70	17.81	16.22	16.48	16.56	14.98	16.61
FeOtot	3.33	2.85	2.37	3.50	2.25	4.21	3.08	2.94	3.01	1.92	2.68
MnO	0.07	0.06	0.07	0.07	0.05	0.08	0.09	0.09	0.09	0.08	0.05
MgO	1.40	1.41	1.32	1.83	0.97	2.54	1.52	1.40	1.30	0.93	1.25
CaO	3.40	3.70	3.25	4.65	2.45	5.35	3.67	3.76	3.76	2.24	3.35
Na_2O	5.00	4.16	4.14	4.03	4.09	4.32	3.81	4.07	4.20	3.16	4.03
K_2O	2.35	3.26	1.80	2.83	3.73	2.14	2.41	3.26	2.86	4.84	3.18
P_2O_5	0.22	0.33	0.20	0.38	0.21	0.34	0.28	0.27	0.29	0.15	0.26
Mg#	42.8	46.8	49.8	48.2	43.4	51.8	46.8	45.9	43.5	46.3	45.4
LOI	-	0.7	0.7	1.5	0.8	1.1	1.2	1.1	1.2	0.7	1.1
Sum	100.8	99.8	99.9	99.7	99.8	99.2	99.8	99.8	99.8	99.9	99.8
XRF											
Sc		9	7	21	9	10	13	10	10	7	10
V	71	47		58	36	100			49		30
Cr	10	27	27	37	26	2	29	29	28	27	29
Ni	4	5	3	17	6	18	9	9	10	6	4
Pb		14	14	12	22	7	31	16	16	32	17
Zr	195	237	139	241	176	283	224	218	250	167	213
Nb	17	19	13	25	15	18	22		20	12	16

Continued

U	3	2	4	4	8	2	2	5	3	2	6
Y	16	16	12	28	14	18	27	14	19	9	12
Th	25	19	14	15	29	15	13		19	8	19
Rb	103	127	152	120	171	73	111	117	118	132	121
Sr	514	558	413	547	431	773	526	555	582	473	530
Ba	505	794	467	670	532	643	599	675	685	987	591
ICP-MS											
Sc											
V			25.0			94.0	54.0	64.0		31.0	
Cr						2.3					
Ni						13.2					
Pb											
Zr			97.4				193.9	184.3			
Hf	5.5		2.8			6.0	5.2	4.7		3.1	
Nb			11.4			15.7	16.3	14.2			
Ta	1.19		0.40			1.00	1.60	1.10		0.90	
U			5.2			3.3	2.8	3.0		2.8	
Y		21.0	10.6			16.6	21.9	14.1		11.0	
Th		25.7	16.1			23.0	14.8	17.2		12.0	
Rb			138.4			77.8	92.8	106.2			
Cs		2.2	11.0			3.1	2.8	2.5		1.8	
Sr			396.0			792.8	479.2	541.5			
Ba			491.0			650.0	625.0	727.0			
La		23.20	23.80			69.60	39.10	41.40		26.79	
Ce		45.98	46.30			136.70	71.70	73.60		48.39	
Pr		5.06	5.30			12.64	7.69	7.58		5.13	
Nd		19.97	19.40			41.60	26.90	26.20		19.67	
Sm	5.10	4.41	3.82			5.91	4.99	4.47		2.80	
Eu	0.98	0.32	0.48			1.30	0.99	0.93		0.64	
Gd		3.75	2.79			4.21	4.06	3.26		2.09	
Tb	0.51		0.38			0.62	0.68	0.49			
Dy		3.50	2.06			3.26	3.81	2.50		1.93	
Ho		0.67	0.34			0.59	0.75	0.51		0.48	
Er		1.75	0.86			1.70	2.21	1.40		1.15	
Tm			0.13			0.26	0.33	0.20			

Continued

Yb	1.17	1.52	0.83	1.55	2.11	1.31	1.10
Lu	0.21	0.21	0.12	0.23	0.33	0.19	0.17
ΣREE		110.3	106.6	280.2	165.7	164.0	
Eu/Eu*		0.2	0.4	0.8	0.7	0.7	0.8
(La/Lu)cn	26.0	11.5	20.6	31.4	12.3	22.6	16.4
(La/Sm)cn	6.5	3.3	3.9	7.4	4.9	5.8	6.0
(Gd/Yb)cn		2.0	2.7	2.2	1.6	2.0	1.5
(Tb/Lu)cn	1.6		2.2	1.8	1.4	1.8	

*1. Major and trace elements from the present study; 2. Major elements, Soldatos *et al.* [18], and trace elements from the present study; 3. Major and trace elements from Soldatos *et al.* [18]; 4. Major and trace elements from Jones *et al.* [17].

Table 2. Isotopic composition of the Elatia pluton samples.

Sample	Type	Reference*	Rb	Sr	87Rb/86Sr	87Sr/86Sr	2σ error	$^{87}Sr/^{86}Sri$	Sm	Nd	$^{147}Sm/^{144}Nd$	$^{143}Nd/^{144}Nd$	2σ error	$^{143}Nd/^{144}Ndi$
PEL-1	Enclave	1	109.4	857.7	0.36899	0.70630	0.000004	0.70600	7.62	46	0.10017	0.51249	0.000004	0.51245
PEL-3	Enclave	1	152.6	674.9	0.65415	0.70710	0.000004	0.70658	5.24	33.1	0.09572	0.51246	0.000004	0.51243
PEL-4	Diorite	1	98.58	1173.53	0.24296	0.70445	0.000004	0.70425	6.27	29.62	0.12798	0.51269	0.000004	0.51264
E-04	Granodiorite	2	105.5	817.7	0.37325	0.70660	0.000003	0.70630	5.85	39.4	0.08977	0.51246	0.000003	0.51242
PS-1	Granodiorite	2	92.8	479.2	0.56025	0.70677	0.000004	0.70633	4.99	26.9	0.11218	0.51246	0.000004	0.51242
DSK-17	Granodiorite	3	85.7	762.0	0.32536	0.70642	0.000130	0.70616	5.64	37.2	0.09167	0.51247	0.000003	0.51244
I-14A	Granodiorite	3	138.4	396.0	1.01114	0.70733	0.000020	0.70653	3.82	19.4	0.11909	0.51236	0.000005	0.51232
PS-03	Granodiorite	3	132	473.0	0.80735	0.70685	0.000070	0.70621	3.1	28	0.06692	0.51245	0.000003	0.51242
PS-11	Granodiorite	3	106.2	541.5	0.56738	0.70669	0.000020	0.70624	4.47	26.2	0.10317	0.51245	0.000004	0.51241
D-5	Granodiorite	3	96	809	0.34200	0.70657	0.000270	0.70630	-	-	-	-	-	-
I-11b	Granodiorite	3	110.83	530.75	0.60400	0.70669	0.000016	0.70621	-	-	-	-	-	-
PS-9	Granodiorite	3	94.72	533.30	0.51380	0.70668	0.000018	0.70627	-	-	-	-	-	-

4.2. Petrography and Mineralogy

The petrography and mineralogy of the Elatia pluton have been extensively discussed by Kotopouli [3], Soldatos [18], and Soldatos *et al.* [19]. In this study, we add new observations on new samples of enclaves, diorite, and granodiorite.

Granodiorite: It consists mainly of (hornblende)-biotite granodiorite, locally ranging from quartz diorite through quartz monzodiorite and tonalite to granite. It is a medium- to coarse-grained, grey to dark grey rock. In the central-western part of the pluton, the granodiorite becomes porphyritic (**Figure 1**) with large K-feldspar megacrysts and displays weak foliation. The porphyritic and non-porphyritic varieties share the same composition and mineralogy. The main rock-forming constituents are plagioclase (33 - 67 vol.%), K-feldspar (7 - 35 vol.%),

quartz (12 - 32 vol.%), and biotite (5 - 22 vol.%). Hornblende (<4 vol.%) is subordinate to the less evolved rocks. Accessory minerals (1 - 6 vol.%) include primary epidote, titanite, allanite, apatite, zircon, and opaque minerals.

Enclaves & Diorite: Generally, scarce scattered enclaves occur in the granodiorite (**Figure 2**); however, an area with many enclaves of different sizes was found during the fieldwork, and a diorite with a septum-like form is found in the granodiorite with moderately smooth contacts. Enclaves and diorite were found in different areas. Both the enclaves and the diorite share the granodiorite mineralogy. They consist mainly of plagioclase (~50%), which displays oscillatory zoning, biotite (15 - 17 vol.%), hornblende (10 - 13 vol.%), minor orthoclase (2 - 3 vol.%), minor quartz (2% - 3%), and accessory minerals such as primary epidote (6 - 8 vol.%), commonly with an allanite core, apatite, and zircon (<4%). Titanite is absent from the enclaves and diorite. Although they present the same mineralogy as the granodiorite, their texture varies slightly, with some displaying a microgranular texture with subhedral biotite, while others exhibit a medium-grained granitic texture. The diorite exhibits a typical granitic texture.

Figure 2. (a) Sample PEL-1, centimeter- to decimeter-sized mafic microgranular enclaves within the granodiorite with moderately sharp contacts, and (b) Sample PEL-2, decimeter-sized mafic microgranular enclaves with gradational contacts within the granodiorite.

4.3. Major Element Geochemistry

Most granodiorite samples plot in and around the granodiorite field, while the enclaves and the diorite plot in the Monzogabbro/Diorite field (**Figure 3**, [28]).

In the SiO_2 – (K_2O + Na_2O) plot (**Figure 4**; [29]), the enclaves and diorite lie in the alkaline field, separated from granodiorite by a SiO_2 gap of more than 7%.

In the SiO_2 versus K_2O diagram (**Figure 5(h)**, after [30]), most samples fall within the High-K calc-alkaline series field, while a few samples plot in the calc-alkaline series. In contrast, the enclaves and diorite plot in the shoshonite series field.

Variation diagrams for major oxides show that most major elements decrease smoothly with increasing SiO_2, exhibiting well-defined trends, except for K_2O, which increases, and Na_2O, which remains nearly constant but tends to decrease

for the granodiorite (Figure 5).

The enclaves generally follow the granodiorite trends, although K_2O and Na_2O diverge, likely due to the SiO_2 gap between the basic enclaves, but diorite diverges from the enclaves in some oxides and especially in TiO_2; thus, the correlation between the granodiorite and enclaves/diorite is not clear. Overall, the major elements variation, at least for the granodiorite, can be attributed to the fractionation of hornblende, biotite, plagioclase, titanite, and apatite.

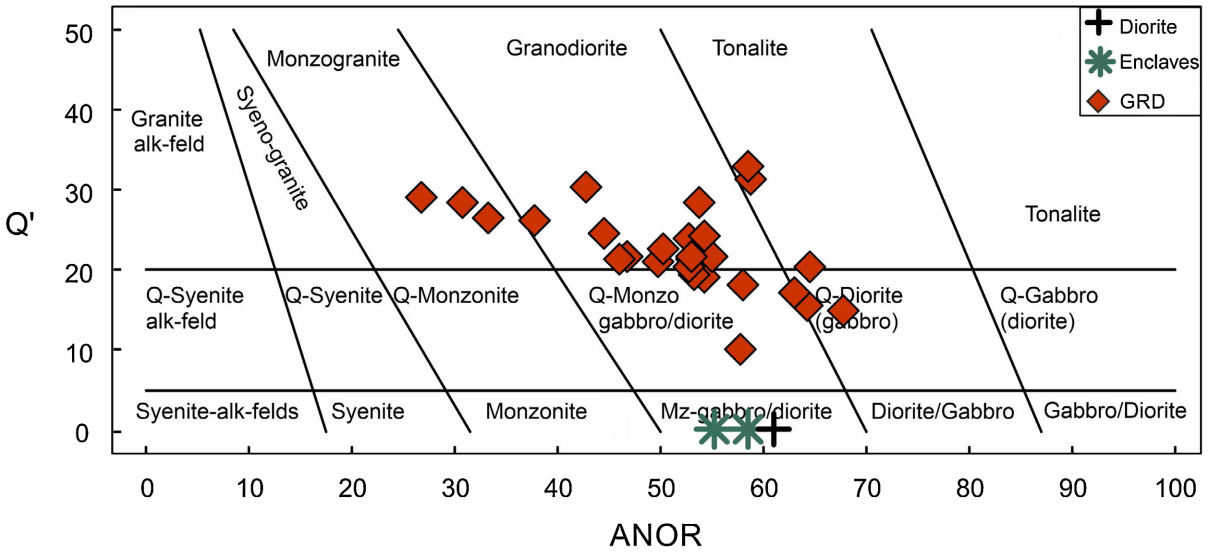

Figure 3. Q-ANOR classification diagram after Streckeisen & Le Maitre [28].

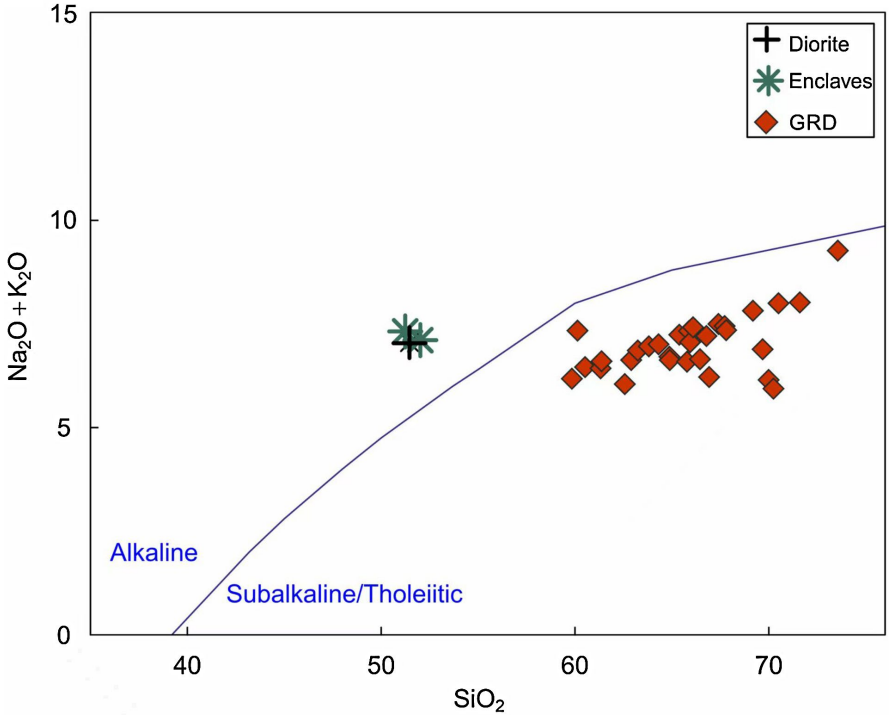

Figure 4. SiO_2 versus $Na_2O + K_2O$ diagram. Discrimination line between alkaline and subalkaline rocks after Irvine & Baragar [29].

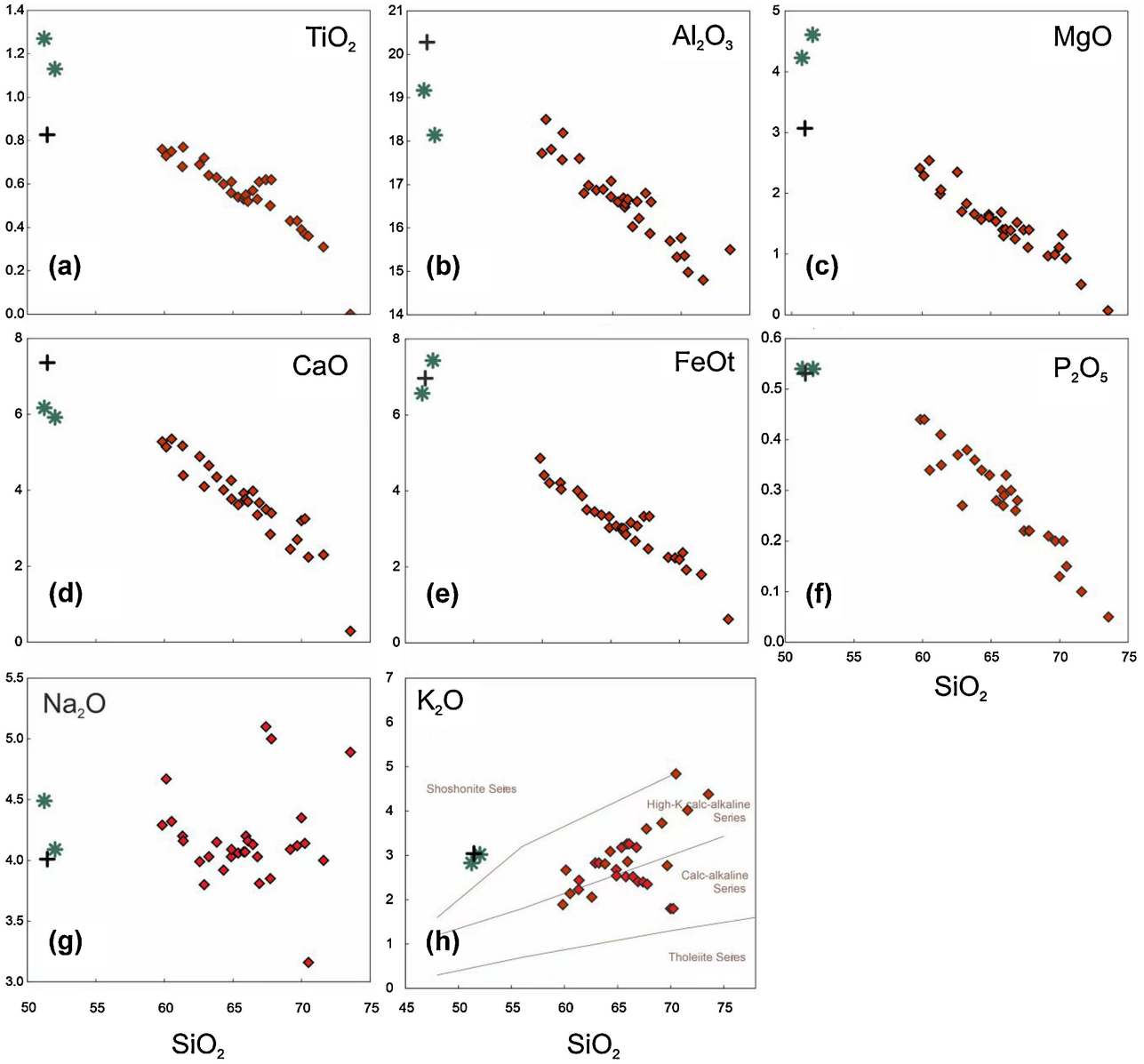

Figure 5. Variation diagrams for major elements. Symbols as in Figure 3.

4.4. Trace Element Geochemistry

Trace-element variation diagrams for selected trace elements are shown in Figure 6. The granodiorite samples correlate well for Sr, V, Pb, and Zr, but less so for Ba, Rb, La, Y, Nb, Pb, Sc, U, and Th. The elements Rb, Pb, U, and Th show an increase with increasing differentiation. Ba, Y, Nb, and Cr variation is more scattered, although they too tend to decrease with differentiation. Th and U are highly scattered; U rises slightly, whereas Th remains relatively constant, decreasing at higher SiO_2 concentrations. The decrease in Y is attributed explicitly to hoblende fractionation [31].

In Figure 7(a), the normalized primitive mantle diagrams for the three rock types display typical convergent-margin generated magmas: variable enrichment

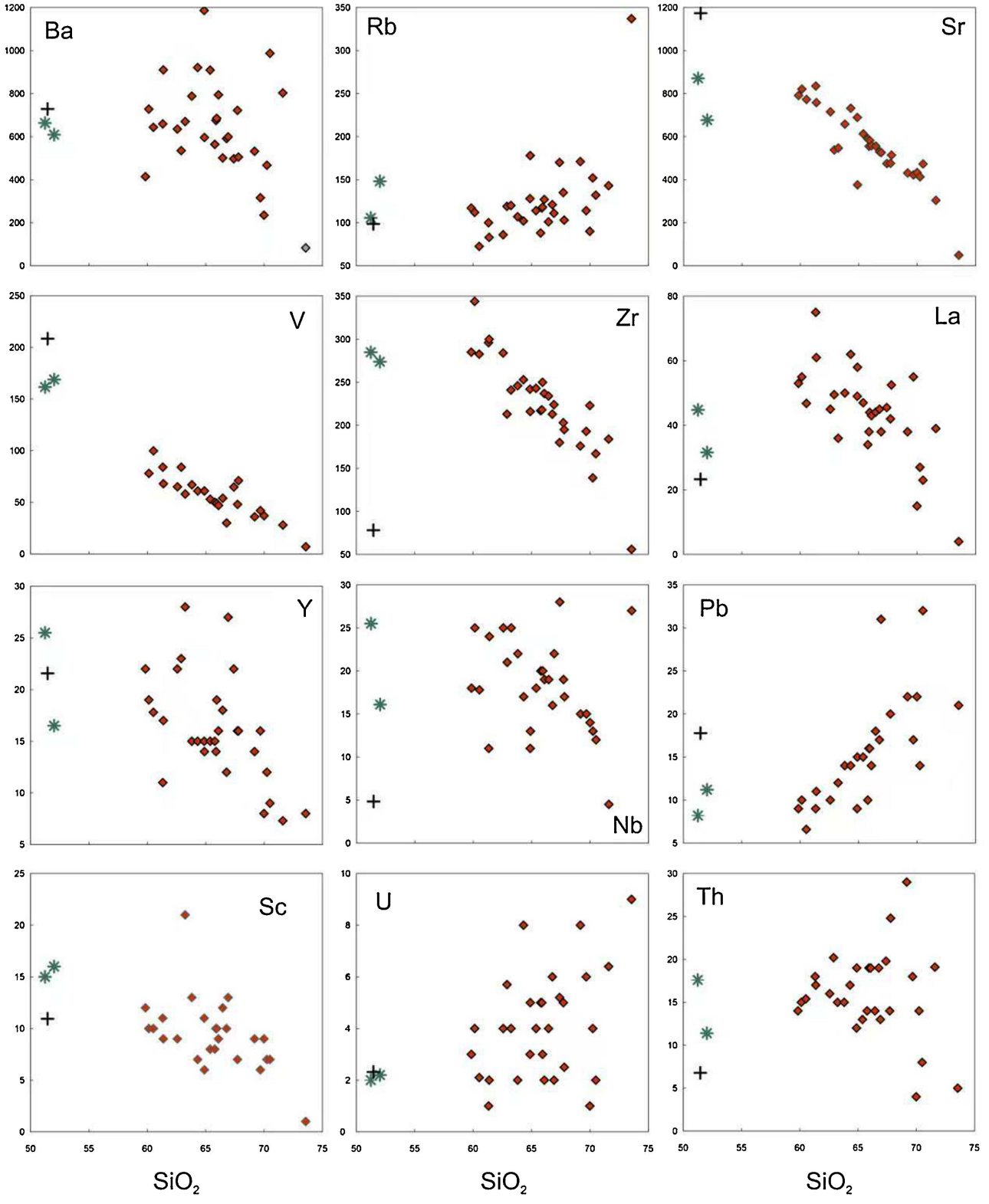

Figure 6. Variation diagrams for selected trace elements. Symbols as in Figure 3.

in LILE (Large-Ion Lithophile Elements), depletion in HFSE (High Field Strength Elements), and negative anomalies in Ta, Nb, Ti, and P, as well as positive anom-

alies in Pb and K. Sr shows variable negative trends. A Ba negative anomaly is present only for granodiorite and enclaves, indicating K-feldspar fractionation, but is absent in diorite. The weak Sr anomaly is probably the result of no or minor plagioclase fractionation during the earlier fractionation stages. The granodiorite also shows a positive Th-U anomaly, whereas the diorite has a negative Th trough. The enclaves display similar patterns to the granodiorite, except for the P and Ti anomalies, which are weaker in the enclaves than in the granodiorite, implying a crustal input.

In Figure 7(b), the chondrite-normalized REE patterns show that the Eu negative anomaly is present, ranging from negligible in the enclaves and diorite to

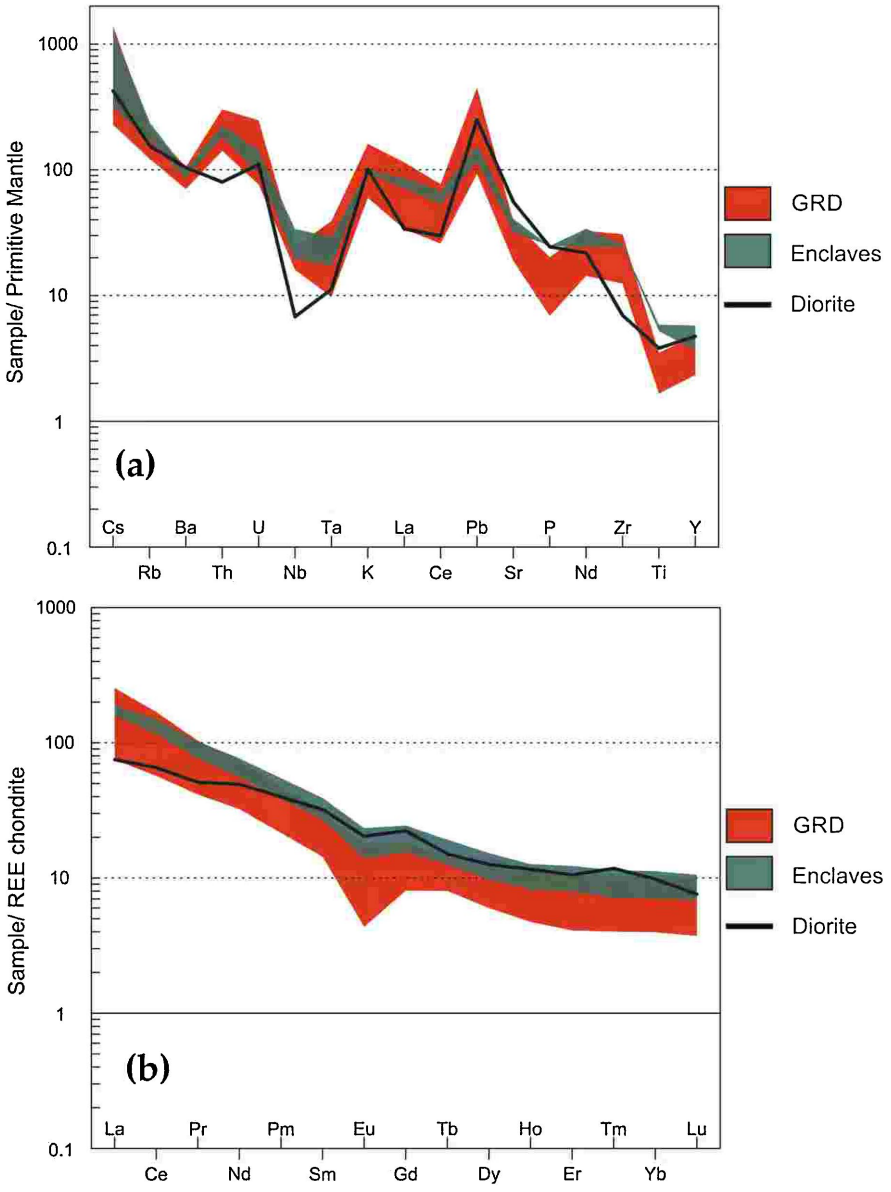

Figure 7. (a) Multi-element spider diagram patterns. Normalization values from Sun & McDonough [35]. (b) REE spider diagram patterns. Normalization values from Boynton [36].

significant in the granodiorite. This, along with the weak Sr anomaly, points to limited plagioclase fractionation. All rocks are LREE-enriched with minor variations ($La_{cn}/Sm_{cn} > 3$), though diorite is slightly less enriched than the others ($La_{cn}/Sm_{cn} = 2.3$). Enclaves and diorite display higher enrichment in HREE than the granodiorite, but all have similar HREE patterns, with $Tb_{cn}/Lu_{cn} > 1$ indicating residual garnet in their source, e.g., Defant and Drummond [31]. There is a notable MREE enrichment in all rock types but especially in the diorite, which reflects strong amphibole fractionation and early titanite fractionation, as both minerals drop towards LREE and HREE, as noted by Padilla *et al.* [32]. The reverse negative Nb-Ta anomaly is an indicator of residual rutile in the source or could reflect source heterogeneity (e.g., [33] [34]).

4.5. Sr and Nd Bulk Rock Isotope Composition

The initial Sr and Nd ratio compositions of the enclaves and granodiorite are similar, whereas the diorite has significantly unradiogenic Sri and radiogenic Ndi ratios (**Figure 8**, **Table 2**). These diorite values indicate a more depleted source, trending toward the depleted mantle (DM) or the European Asthenospheric Reservoir (EAR). The remaining samples plot between this depleted end-member and enriched crustal values, consistent with mixing between a mantle-derived melt and a crustal melt. Because the enclaves share mineralogy with the diorite, they likely represent mixtures of a depleted melt component (diorite-like) and a

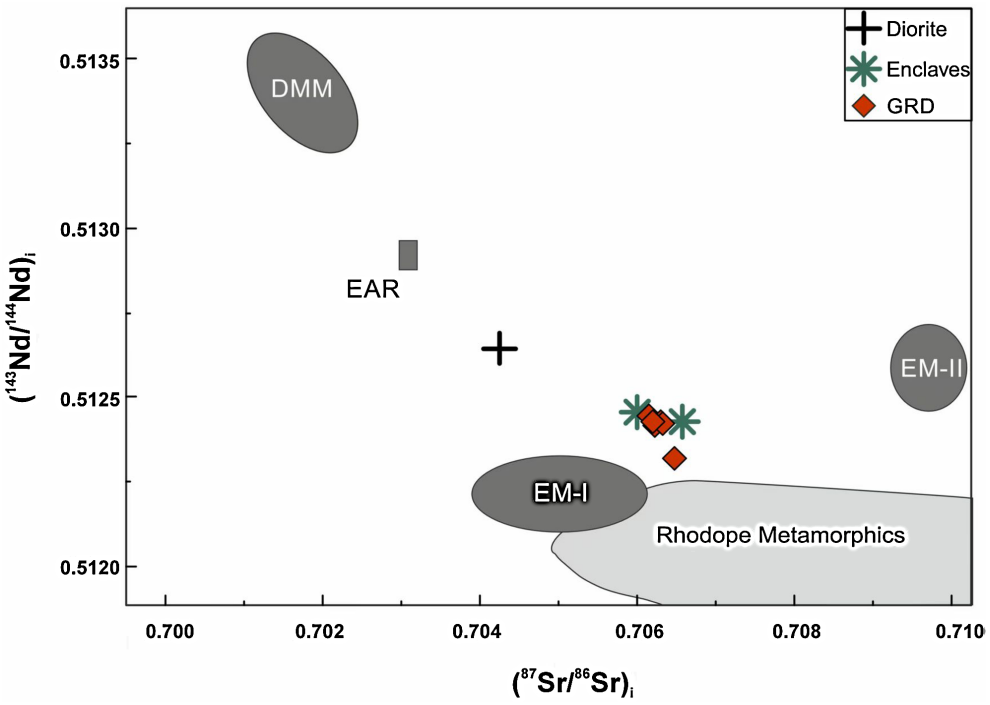

Figure 8. (87Sr/86Sr)i versus (143Nd/144Nd)i. The fields illustrated are: DMM = Depleted MORB Mantle, EM-I = Enriched Mantle I, EM-II = Enriched Mantle II after Zindler & Hart [37]. EAR = European Asthenospheric Reservoir after Cebria & Wilson [38], Rhodope metamorphics after Cornelius [39] and Castorina *et al.* [40].

high Sri, low Ndi melt component, probably derived from the Jurassic metamorphic rocks of the RMC crust.

4.6. Geotectonic Discrimination Diagrams

Many authors have worked to update classic tectonic-discrimination diagrams, replacing hand-drawn boundaries with more rigorous decision boundaries based on discrimination analysis, which provides very good probabilities. Pearce himself [41] revised the Rb/Y + Nb discrimination diagram (**Figure 9**, [42]). Verma and Verma [43] developed three sets of discrimination diagrams using the correct statistical methodology of loge-ratio transformation and linear discrimination analysis with a high success rate (>90%). All intermediate samples of the current study were plotted in these diagrams (**Figure 10**). All samples are plotted in the "Col" field, which is discriminated using samples from post-collisional tectonic environments. Thus, a post-collisional setting is suggested for the Elatia pluton rather than a pre-collision one.

5. Discussion

5.1. Origin of the Diorite

The diorite outcrop is small, and such samples are rare within the Rhodope magmatic rocks. This specimen is rather significant among all plutons of the RMC. Although it is represented by a single, and thus less statistically reliable, sample,

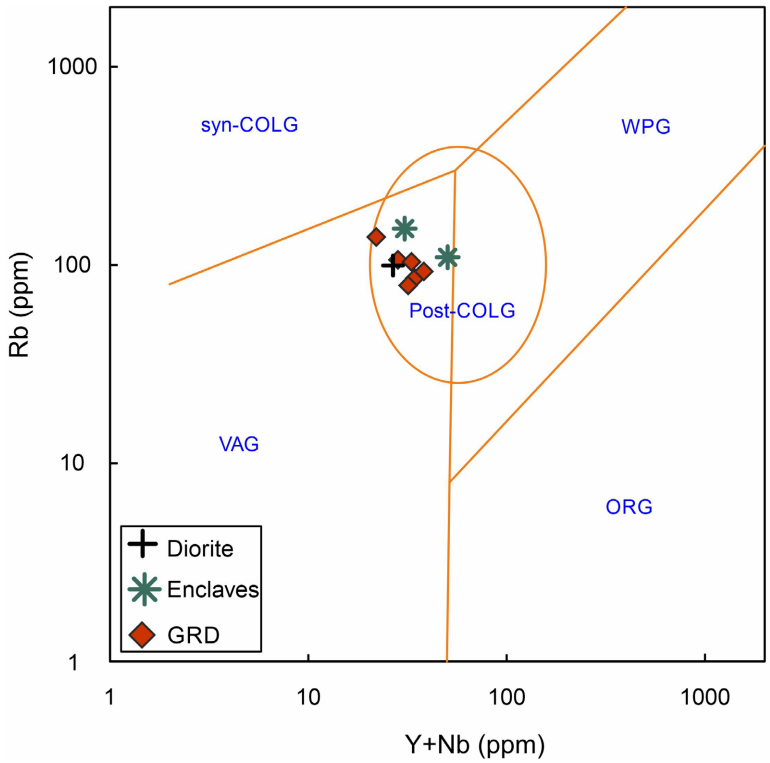

Figure 9. Rb versus Y + Nb discrimination diagram of geotectonic settings (after Pearce *et al.* [42], modified by Pearce [41]).

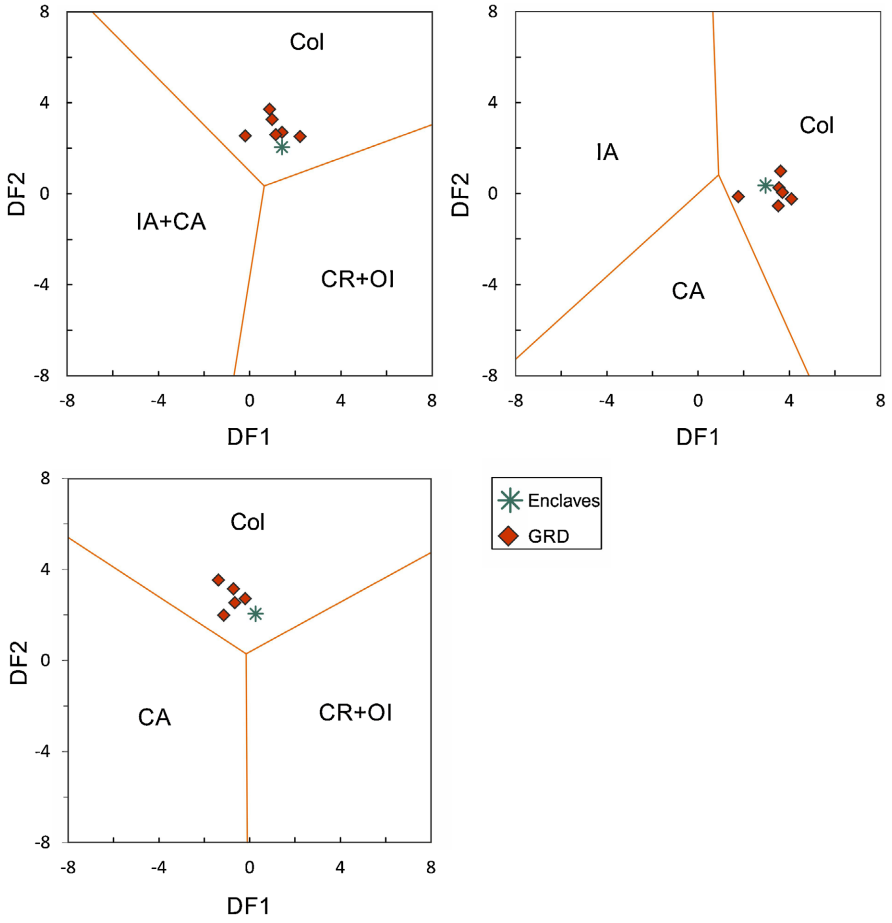

Figure 10. Tectonic discrimination diagrams for intermediate magmas according to Verma & Verma [43]. Col = Collisional Settings; IA + CA = Island Arc & Continental Arc; CR + OI = Continental Rift & Oceanic Islands; IA = Island Arc; CA = Continental Arc; CR = Continental Rift & Oceanic Island. SiO_2 range: 52 - 63 wt.%.

it remains noteworthy and cannot be disregarded. Its unradiogenic Sr isotopic ratio and radiogenic eNd (+1.5) point to melt originating from a depleted mantle source. The alkaline affinity of the diorite suggests that the melt formed by high degrees of partial melting of a volumetrically minor mantle component [34]. The weak Eu and Sr anomalies suggest minor or no plagioclase fractionation, while the MREE shift points to strong amphibole fractionation. The negative Th anomaly combined with the reversed Nb-Ta anomaly strongly suggests residual rutile in the source, as rutile prefers Ta over Nb (e.g., [35] [36]). At the same time, the sample has enriched features like the high-K, low Mg# (=44) and LILE and HFSE enrichment. Such signatures typically occur only when the mantle wedge is metasomatized by sediment-derived melts or slab-released fluids during subduction from the subducted slab. To explain the depleted isotopic character for some RMC magmatics, Rohrmeier *et al.* [7], working on the Yugovo and Smilyan plutons, suggested the possibility of a Variscan melt component, which Marchev *et al.* [44] accepted. However, these authors link the depleted isotopic character to a Variscan component in some RMC magmatics due to the limited data for Early-Mid-

dle Eocene mafic members. A Variscan component is highly unlikely here, indicated by the high εNd (+1.5), and excludes any scenario for significant Variscan contribution. Its low Mg# here can only be attributed to the amphibole cumulates of the Elatia pluton (Soldatos personal communication). An analyzed sample from these cumulates found in the Elatia pluton shows high 13.36 MgO w% and low K_2O (1.09 w%; Soldatos unpublished data). Crystal-liquid separation within the Elatia magma chamber would have depleted the residual melt. Since a Variscan component is excluded, the only plausible explanation for the origin of the diorite is an enriched mantle melt component depleted in MgO due to the amphibole cumulate rocks.

5.2. Origin of the Enclaves and Granodiorite

The diorite and the mafic enclaves do not crop out in the same part of the Elatia pluton. Titanite is present in the enclaves but is absent from the diorite. Amphibole fractionation plays a major role for the granodiorite as implied by the Y variation. In most variation diagrams (**Figure 5** and **Figure 6**), both for major and trace elements, the enclaves have a subparallel trend; however, with only two samples it is not sufficient to draw conclusions. Moreover, the gap in SiO_2 is a deterrent factor for any conclusions. The Mg# ranges between ~45 - 51 for the granodiorite and 52.5 - 53.4 for the enclaves, typical of magmas in arc settings, signaling moderately evolved magmas. Relative to the diorite, they are more enriched in LILE and HSFE (**Figure 7**), and their trace element and REE patterns resemble those of the granodiorite, suggesting a strong connection. Their initial isotopic ratios are the same as the granodiorite, 0.70600 - 0.70658 and 0.70621 - 0.70653, respectively. Their features point to a formation from significant mixing with concurrent FC between the diorite magma and a felsic melt component, none other than the crust of the RMC as indicated by the Sr and Nd initial isotopic ratios (**Figure 8**). The granodiorite itself seems to represent the result of this mixing with concurrent FC (MFC) between the diorite magma and a felsic RMC crustal melt. In short, both the enclaves and the granodiorite could probably record successive stages of diorite-crustal melt and then enclave-crustal melt interaction with concurrent FC.

5.3. Evolution of the Pluton

Previous authors have utilized geochemical models to explore the evolutionary processes and the relationship between the granodiorite, the granite, and the two-mica granite [17] [18]. No earlier work, however, addressed the enclaves or the diorite. Enclave mineralogy resembles that of the granodiorite, although the enclaves exhibit varying textures. Mineral chemistry shows no compositional differences among the granodiorite, the enclaves, and the diorite. Major element variations imply a relation with the granodiorite, but their trace element variations, especially for the diorite, are not consistent. Even so, trace element and REE spider diagrams indicate a strong relation between the enclaves and granodiorite. The

diorite differs in detail; yet the continuous depletion with differentiation of their HREE, the similar HREE patterns, and their constant upward shift on the MREE, caused by strong hornblende fractionation, strongly support a common evolution. Amphibole fractionation appears to play a key role, as indicated by the high Sm_{cn}/Dy_{cn} ratio (>2) and the low Dy_{cn}/Yb_{cn} ratio (<1.6), along with a moderate Sr/Y ratio with garn*et al*so present in the residue. The amphibole cumulates further support this view. Amphibole fractionation, along with epidote and allanite, is also the driving mechanism of the pluton's "adakitic" signature [45], lowering the Y and Yb concentrations and further generating adakites [46]. The term adakite is used to describe a group of rocks with high Sr and low Y and HREE concentrations and high Sr/Y and La/Yb ratios considered to be the product of slab melting in subduction zone settings (**Figure 11**; [47]), yet such a signature can be achieved via different processes: melting of a high Sr/Y (and La/Yb) source; deep melting, with abundant residual garnet; fractional crystallization or assimilation and fractional crystallization; or interactions of felsic melts with the mantle, causing selective enrichment in LREE and Sr over HREE [48]. These "adakites" are the direct result of high-pressure melts (*i.e.*, >10 Kbar) of different sources; as the pressure increases, plagioclase becomes unstable (therefore releasing Sr), whereas garnet becomes stable and an increasingly important phase, trapping Y. The result is a dramatic increase of the Sr/Y ratio with increasing pressure; La and Yb have comparable behaviors, such that the La/Yb ratio shows the same pattern [49].

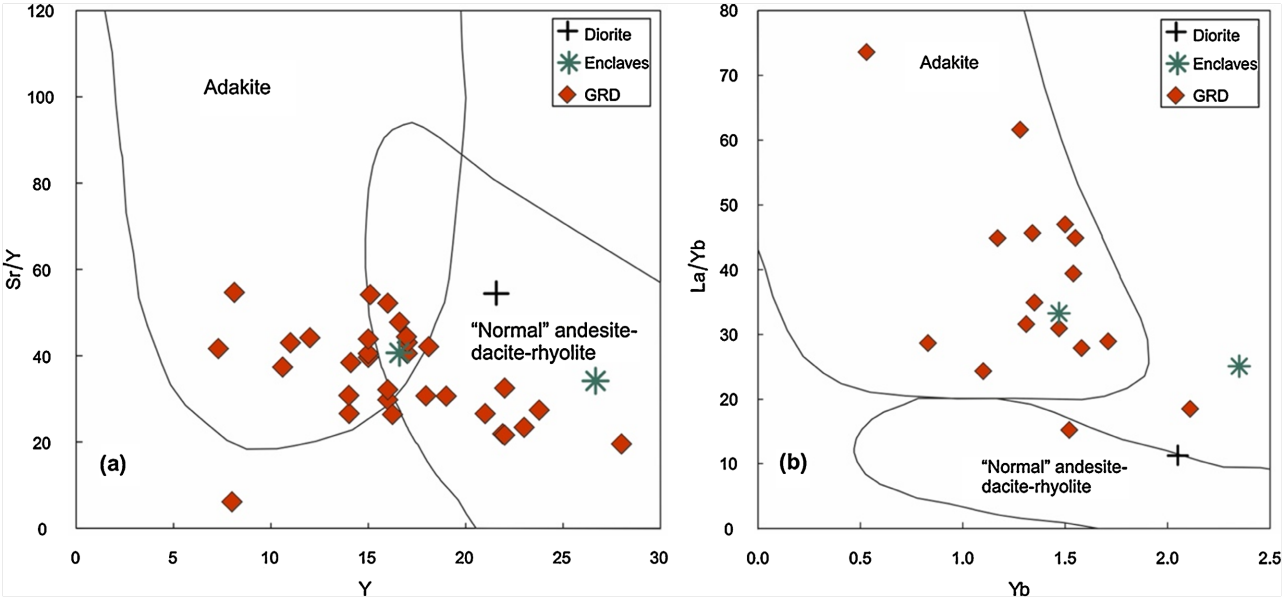

Figure 11. Discrimination diagram of adakites (a) Y versus Sr/Y and (b) Yb versus La/Yb. Fields from [49].

The role of the mafic members, especially the diorite, is key to understanding the origin of the Elatia pluton. Their alkaline character suggests origin from high degrees of melting of a volumetrically minor mantle component [50]. The initial Sr and Nd isotopic ratios of the enclaves are similar to those of granodiorite, con-

firming extensive mixing. Nonetheless, the diorite displays more depleted REE and trace element patterns, with very low initial Sr and high Nd representing the most primitive magma composition yet identified in the Hellenic RMC. Its enriched incompatible elements, depletion in some compatible elements (**Figure 7(a)**), and the low Mg# relative to the enclaves (44 versus 52.5 and 53.4) suggest that it has probably been subjected to a complex differentiation process, probably linked to the cumulitic amphibole diorite outcrops (Soldatos personal communication) noted in the area. The cumulates consist mainly of amphiboles (Soldatos, personal communication) with very low SiO_2, very low K_2O, and high Mg# (=75). They are enriched in compatible elements yet require further investigation. Nevertheless, its isotopic signature is reliable, as differentiation processes cannot erase it. If future work confirms a link between the diorite and the cumulates, then the answer for the selective depletion seen in the diorite could be explained. At present, data on these cumulates are limited, and the diorite sample found in this study's field work remains unique. Undoubtedly, the enclaves demonstrate a mantle-derived origin, although they have been subjected to mixing with a crustal melt component [50], consistent with their high MgO content.

For the origin of the Early-Middle Eocene magmatism in RMC, Marchev *et al.* [44] proposed melts derived from an enriched mantle source with varying degrees of crustal contamination from the metamorphic rocks of the Middle Allochthon of RMC (Sidironero Unit). Christofides *et al.* [51], studying the 50 Ma Sithonia Plutonic Complex, where enclaves are also present, suggested an Upper Mantle origin component, though Perugini *et al.* [52] argued that extensive mixing limited the source information. Earlier studies proposed assimilation and FC (AFC) as the main differentiation process linking the less- and more-differentiated granodiorite [18]. The presence of numerous enclaves and diorite, however, points to a mixing process with concurrent FC rather than crustal assimilation. In the Elatia pluton, the isotopic signatures of both felsic rocks and enclaves are in favor of mixing between a mantle-derived melt and a crustal melt component. A two-stage evolution is suggested here, MFC between a diorite magma with felsic RMC crustal melt that generated the enclaves, and continuous mixing and FC that generated the granodiorite.

5.4. Geotectonic Setting and Geodynamic Implications

Several authors have discussed the geotectonic setting of the Elatia pluton. All of them support a subduction-related environment based on several geotectonic discrimination diagrams, with some supporting a pre-collision environment [18] and others a post-collision one [17] [44].

Recently, the validity of previously used discrimination diagrams has been called into question, as the decision boundaries of most tectonic discrimination diagrams are typically drawn by eye [53]. Pearce himself revised his key diagram of Rb/Y + Nb [42], adding a post-collision field [41]. This discrimination diagram, along with that of Verma and Verma [43], has been used to determine the post-

collision geotectonic setting of the Elatia pluton. Both diagrams clearly show the post-collisional character of the pluton. The Elatia pluton, along with the other Eocene plutonic complexes of RMC, intruded its crust shortly after the closure of the Vardar-Axios zone, presenting "adakitic" characteristics unlike the other younger post-collision plutons.

Many authors have dated the closure of the Axios-Vardar ocean, with many of them suggesting a Late Cretaceous-Paleocene age (e.g. [54]-[58]), while some imply that convergence persisted into the Eocene-Oligocene (e.g. [10] [59]). The Elatia pluton, as many previous workers agreed and as shown in this study, is a post-collisional one and was emplaced around 56 Ma; therefore, the oceanic crust must have been fully consumed no later than the latest Paleocene, before the pluton was emplaced.

6. Conclusions

The new field petrographic and geochemical data show that the granodiorite of the Elatia pluton evolved through intense mixing between an enriched mantle-derived magma and a crustal melt derived from the local Rhodopean crust. Extensive amphibole fractionation, with limited plagioclase fractionation, and high-degree partial melting with residual rutile in the mantle source control the origin and evolution of the mafic diorite member. Intense MFC between the mafic diorite source melt and an RMC crustal melt, with crystallization of hornblende, biotite, plagioclase, titanite, and apatite, appears to be the controlling mechanism for the enclave origin and the genesis and evolution of the Elatia pluton granodiorite. Evidence for the mantle component is preserved in the rare diorite, whose very low Sri (0.7042) and positive εNd (+1.5) lie outside the range of the surrounding metamorphic rocks; all other samples plot on straight-line trends that connect the mantle member with RMC crustal isotopic signatures, confirming the hybrid origin of the granodiorite.

When the samples are tested using statistically defined discrimination diagrams, particularly those for intermediate rocks by Verma and Verma [43], all samples fall within the collision field and are in agreement with the revised Rb-Y + Nb plot. Coupled with the zircon U-Pb age of about 56 Ma and the limited contact metamorphism imposed on the host rocks, these geochemical classifications indicate emplacement during the early post-collision period that followed the end of subduction in the Rhodope, rather than during a pre- or syn-collision stage as proposed in earlier studies.

Overall, the Elatia pluton can be regarded as a prime example of early Eocene post-collisional magmatism in the RMC. Recognizing the key role of mantle-crust magma mixing, constrained by the distinctive diorite mafic end-member, provides a coherent framework for the evolution of the Elatia pluton. Further study of the diorite, enclaves, and amphibole cumulates could clarify the differentiation history of the diorite and help identify the crustal component that mixed with it, thereby better explaining the origin of the granodiorite.

Acknowledgements

I sincerely thank the anonymous reviewers for their careful reading, insightful comments, and constructive suggestions, all of which significantly improved the clarity and quality of this manuscript. I am grateful to Prof. Triantafyllos Soldatos (A.U.Th.) for providing the Elatia pluton samples, data on the amphibole cumulates, and many insightful discussions. I also thank Prof. Antonios Koroneos (A.U.Th.), Emeritus Prof. Georgios Christofides (A.U.Th.), Prof. Lamprini Papadopoulou (A.U.Th.), Prof. Giampiero Poli (University of Perugia), and Prof. Georgia Pe-Piper (Saint Mary's University, Halifax) for their guidance and continual support, and my friend Dr. Anna Bourliva (A.U.Th.) for her valuable assistance.

Funding

This research has been co-financed by the European Union (European Social Fund—ESF) and Greek national funds through the Operational Program "Education and Lifelong Learning" of the National Strategic Reference Framework (NSRF)-Research Funding Program: Heracleitus II. Investing in a knowledge society through the European Social Fund.

Conflicts of Interest

The author declares no conflicts of interest regarding the publication of this paper.

References

[1] Brun, J.-P. and Sokoutis, D. (2007) Kinematics of the Southern Rhodope Core Complex (North Greece). *International Journal of Earth Sciences*, **96**, 1079-1099. https://doi.org/10.1007/s00531-007-0174-2

[2] Burg, J.P. (2012) Rhodope: From Mesozoic Convergence to Cenozoic Extension. Review of Petro-Structural Data in the Geochronological Frame. *Journal of the Virtual Explorer*, **42**, 1-44. https://doi.org/10.3809/jvirtex.2011.00270

[3] Kotopouli, C.N. (1981) The Magmatic Rocks in the Area of Skaloti-Paranesti, Greek Rhodope. Doctoral Dissertation, University of Patras.

[4] Sklavounos, S. (1981) The Paranesti Granite: Mineralogy and Petrography. Doctoral Dissertation, Aristotle University of Thessaloniki.

[5] Soldatos, T. (1985) Petrology and Geochemistry of the Elatia Pluton. Doctoral Dissertation, Aristotle University of Thessaloniki.

[6] Froitzheim, N., Jahn-Awe, S., Frei, D., Wainwright, A.N., Maas, R., Georgiev, N., *et al.* (2014) Age and Composition of Meta-Ophiolite from the Rhodope Middle Allochthon (Satovcha, Bulgaria): A Test for the Maximum-Allochthony Hypothesis of the Hellenides. *Tectonics*, **33**, 1477-1500. https://doi.org/10.1002/2014tc003526

[7] Rohrmeier, M.K., von Quadt, A., Driesner, T., Heinrich, C.A., Handler, R., Ovtcharova, M., *et al.* (2013) Post-Orogenic Extension and Hydrothermal Ore Formation: High-Precision Geochronology of the Central Rhodopian Metamorphic Core Complex (Bulgaria-Greece). *Economic Geology*, **108**, 691-718. https://doi.org/10.2113/econgeo.108.4.691

[8] Mposkos, E. and Krohe, A. (2000) Petrological and Structural Evolution of Continen-

tal High-Pressure Metamorphic Rocks in the Alpine Rhodope Domain (N. Greece). In: Panayides, I., Xenophontos, C. and Malpas, J., Eds., *Proceedings of the 3rd International Conference on the Geology of the Eastern Mediterranean*, Geological Survey Department, 221-232.

[9] Turpaud, P. and Reischmann, T. (2009) Characterisation of Igneous Terranes by Zircon Dating: Implications for UHP Occurrences and Suture Identification in the Central Rhodope, Northern Greece. *International Journal of Earth Sciences*, **99**, 567-591. https://doi.org/10.1007/s00531-008-0409-x

[10] Jahn-Awe, S., Froitzheim, N., Nagel, T.J., Frei, D., Georgiev, N. and Pleuger, J. (2010) Structural and Geochronological Evidence for Paleogene Thrusting in the Western Rhodopes, SW Bulgaria: Elements for a New Tectonic Model of the Rhodope Metamorphic Province. *Tectonics*, **29**, TC3008. https://doi.org/10.1029/2009tc002558

[11] Ricou, L., Burg, J., Godfriaux, I. and Ivanov, Z. (1998) Rhodope and Vardar: The Metamorphic and the Olistostromic Paired Belts Related to the Cretaceous Sub-Duction under Europe. *Geodinamica Acta*, **11**, 285-309. https://doi.org/10.1016/S0985-3111(99)80018-7

[12] Kydonakis, K., Brun, J., Sokoutis, D. and Gueydan, F. (2015) Kinematics of Cretaceous Subduction and Exhumation in the Western Rhodope (Chalkidiki Block). *Tectonophysics*, **665**, 218-235. https://doi.org/10.1016/j.tecto.2015.09.034

[13] Mposkos, E. and Krohe, A. (2006) Pressure-Temperature-Deformation Paths of Closely Associated Ultra-High-Pressure (Diamond-Bearing) Crustal and Mantle Rocks of the Kimi Complex: Implications for the Tectonic History of the Rhodope Mountains, Northern Greece. *Canadian Journal of Earth Sciences*, **43**, 1755-1776. https://doi.org/10.1139/e06-064

[14] Georgiev, N., Pleuger, J., Froitzheim, N., Sarov, S., Jahn-Awe, S. and Nagel, T.J. (2010) Separate Eocene-Early Oligocene and Miocene Stages of Extension and Core Complex Formation in the Western Rhodopes, Mesta Basin, and Pirin Mountains (Bulgaria). *Tectonophysics*, **487**, 59-84. https://doi.org/10.1016/j.tecto.2010.03.009

[15] Burg, J., Ricou, L., Ivano, Z., Godfriaux, I., Dimov, D. and Klain, L. (1996) Synmetamorphic Nappe Complex in the Rhodope Massif. Structure and Kinematics. *Terra Nova*, **8**, 6-15. https://doi.org/10.1111/j.1365-3121.1996.tb00720.x

[16] Kilias, A., Vamvaka, A., Fassoulas, C., Falalakis, G., Avgerinas, S., Sfeikos, A., Pipera, K., Katrivanos, E. and Thomaidou, E. (2016) A Geological Cross-Section through Northern Greece from the Pindos to Rhodope Mountain Ranges: A Field Guide across the External and Internal Hellenides. *Journal of the Virtual Explorer*, **50**, 1-107. https://doi.org/10.3809/jvirtex.2016.08685

[17] Jones, C.E., Tarney, J., Baker, J.H. and Gerouki, F. (1992) Tertiary Granitoids of Rhodope, Northern Greece: Magmatism Related to Extensional Collapse of the Hellenic Orogen? *Tectonophysics*, **210**, 295-314. https://doi.org/10.1016/0040-1951(92)90327-3

[18] Soldatos, T., Koroneos, A., Christofides, G. and Del Moro, A. (2001) Geochronology and Origin of the Elatia Plutonite (Hellenic Rhodope Massif, N. Greece) Constrained by New Sr Isotopic Data. *Neues Jahrbuch für Mineralogie-Abhandlungen*, **176**, 179-209. https://doi.org/10.1127/njma/176/2001/179

[19] Soldatos, T., Koroneos, A., Kamenov, B. K., Peytcheva, I., von Quadt, A., Christofides, G., Zheng, X. and Sang, H. (2008) New U-Pb and Ar-Ar Mineral Ages for the Barutin-Buynovo-Elatia-Skaloti-Paranesti Batholith (Bulgaria and Greece): Refinement of Its Debatable Age. *Geochemistry, Mineralogy and Petrology*, **46**, 85-102.

[20] Batchelor, R.A. and Bowden, P. (1985) Petrogenetic Interpretation of Granitoid Rock

Series Using Multicationic Parameters. *Chemical Geology*, **48**, 43-55. https://doi.org/10.1016/0009-2541(85)90034-8

[21] Harris, N.B.W., Pearce, J.A. and Tindle, A.G. (1986) Geochemical Characteristics of Collision-Zone Magmatism. In: Coward, M.P. and Ries, A.C., Eds., *Collision Tectonics*, Geological Society Special Publication 19, 67-81. https://doi.org/10.1144/gsl.sp.1986.019.01.04

[22] Eggins, S.M. (2003) Laser Ablation ICP-MS Analysis of Geological Materials Prepared as Lithium Borate Glasses. *Geostandards Newsletter*, **27**, 147-162. https://doi.org/10.1111/j.1751-908x.2003.tb00642.x

[23] Longerich, H.P., Jackson, S.E. and Günther, D. (1996) Inter-Laboratory Note. Laser Ablation Inductively Coupled Plasma Mass Spectrometric Transient Signal Data Acquisition and Analyte Concentration Calculation. *Journal of Analytical Atomic Spectrometry*, **11**, 899-904. https://doi.org/10.1039/ja9961100899

[24] van Achterberg, E., Ryan, C., Jackson, S. and Griffin, W. (2001) Data Reduction Software for LAICPMS. In: Sylvester, P.J., Ed., *Laser Ablation ICPMS in the Earth Sciences*: *Principles and Applications*, Mineralogical Association of Canada, Short Course Series 29, 239-243.

[25] Michard, A., Gurriet, P., Soudant, M. and Albarede, F. (1985) Nd Isotopes in French Phanerozoic Shales: External Vs. Internal Aspects of Crustal Evolution. *Geochimica et Cosmochimica Acta*, **49**, 601-610. https://doi.org/10.1016/0016-7037(85)90051-1

[26] Janoušek, V., Farrow, C.M. and Erban, V. (2006) Interpretation of Whole-Rock Geochemical Data in Igneous Geochemistry: Introducing Geochemical Data Toolkit (GCDkit). *Journal of Petrology*, **47**, 1255-1259. https://doi.org/10.1093/petrology/egl013

[27] Petrelli, M., Poli, G., Perugini, D. and Peccerillo, A. (2005) Petrograph: A New Software to Visualize, Model, and Present Geochemical Data in Igneous Petrology. *Geochemistry*, *Geophysics*, *Geosystems*, **6**, Q07011. https://doi.org/10.1029/2005gc000932

[28] Streckeisen, A. and Le Maitre, R.W. (1979) A Chemical Approximation to the Modal QAPF Classification of Igneous Rocks. *Neues Jahrbuch für Mineralogie-Abhandlungen*, **136**, 169-206.

[29] Irvine, T.N. and Baragar, W.R.A. (1971) A Guide to the Chemical Classification of the Common Volcanic Rocks. *Canadian Journal of Earth Sciences*, **8**, 523-548. https://doi.org/10.1139/e71-055

[30] Peccerillo, A. and Taylor, S.R. (1976) Geochemistry of Eocene Calc-Alkaline Volcanic Rocks from the Kastamonu Area, Northern Turkey. *Contributions to Mineralogy and Petrology*, **58**, 63-81. https://doi.org/10.1007/bf00384745

[31] Defant, M.J. and Drummond, M.S. (1990) Derivation of Some Modern Arc Magmas by Melting of Young Subducted Lithosphere. *Nature*, **347**, 662-665. https://doi.org/10.1038/347662a0

[32] Padilla, A.J. and Gualda, G.A.R. (2016) Crystal-Melt Elemental Partitioning in Silicic Magmatic Systems: An Example from the Peach Spring Tuff High-Silica Rhyolite, Southwest USA. *Chemical Geology*, **440**, 326-344. https://doi.org/10.1016/j.chemgeo.2016.07.004

[33] Foley, S.F., Barth, M.G. and Jenner, G.A. (2000) Rutile/Melt Partition Coefficients for Trace Elements and an Assessment of the Influence of Rutile on the Trace Element Characteristics of Subduction Zone Magmas. *Geochimica et Cosmochimica Acta*, **64**, 933-938. https://doi.org/10.1016/s0016-7037(99)00355-5

[34] Schmidt, M.W., Dardon, A., Chazot, G. and Vannucci, R. (2004) The Dependence of

Nb and Ta Rutile-Melt Partitioning on Melt Composition and Nb/Ta Fractionation during Subduction Processes. *Earth and Planetary Science Letters*, **226**, 415-432. https://doi.org/10.1016/j.epsl.2004.08.010

[35] Sun, S.S. and McDonough, W.F. (1989) Chemical and Isotopic Systematics of Oceanic Basalts: Implications for Mantle Composition and Processes. In: Saunders, A.D. and Norry, M.J., Eds., *Magmatism in Ocean Basins*, Geological Society Special Publication 42, 313-345. https://doi.org/10.1144/gsl.sp.1989.042.01.19

[36] Boynton, W.V. (1984) Cosmochemistry of the Rare Earth Elements: Meteorite Studies. In: Henderson, P., Ed., *Rare Earth Element Geochemistry*, Elsevier, 63-114. https://doi.org/10.1016/b978-0-444-42148-7.50008-3

[37] Zindler, A. and Hart, S. (1986) Chemical Geodynamics. *Annual Review of Earth and Planetary Sciences*, **14**, 493-571. https://doi.org/10.1146/annurev.ea.14.050186.002425

[38] Cebriá, J.M. and Wilson, M. (1995) Cenozoic Mafic Magmatism in Western/Central Europe: A Common European Asthenospheric Reservoir. *Terra Nova*, **7**, 162.

[39] Cornelius, N.K. (2008) UHP Metamorphic Rocks of the Eastern Rhodope Massif, NE Greece: New Constraints from Petrology, Geochemistry, and Zircon Ages. Doctoral Dissertation, University of Mainz. https://doi.org/10.25358/openscience-4327

[40] Castorina, F., Koroneos, A., Masi, U. and Eleftheriadis, G. (2014) Geochemical and Sr-Nd Isotopic Evidence for Origin and Evolution of the Miocene Pangeon Granitoids, Southern Rhodope, Greece. *International Geology Review*, **56**, 622-652. https://doi.org/10.1080/00206814.2014.883490

[41] Pearce, J.A., Harris, N.B.W. and Tindle, A.G. (1984) Trace Element Discrimination Diagrams for the Tectonic Interpretation of Granitic Rocks. *Journal of Petrology*, **25**, 956-983. https://doi.org/10.1093/petrology/25.4.956

[42] Pearce, J.A. (1996) Sources and Settings of Granitic Rocks. *Episodes*, **19**, 120-125. https://doi.org/10.18814/epiiugs/1996/v19i4/005

[43] Verma, S.P. and Verma, S.K. (2013) First 15 Probability-Based Multidimensional Tectonic Discrimination Diagrams for Intermediate Magmas and Their Robustness against Postemplacement Compositional Changes and Petrogenetic Processes. *Turkish Journal of Earth Sciences*, **22**, 931-995. https://doi.org/10.3906/yer-1204-6

[44] Marchev, P., Georgiev, S., Raicheva, R., Peytcheva, I., von Quadt, A., Ovtcharova, M., *et al.* (2013) Adakitic Magmatism in Post-Collisional Setting: An Example from the Early-Middle Eocene Magmatic Belt in Southern Bulgaria and Northern Greece. *Lithos*, **180-181**, 159-180. https://doi.org/10.1016/j.lithos.2013.08.024

[45] Xu, W., Zhang, H., Luo, B., Guo, L. and Yang, H. (2015) Adakite-Like Geochemical Signature Produced by Amphibole-Dominated Fractionation of Arc Magmas: An Example from the Late Cretaceous Magmatism in Gangdese Belt, South Tibet. *Lithos*, **232**, 197-210. https://doi.org/10.1016/j.lithos.2015.07.001

[46] Zhang, L., Li, S. and Zhao, Q. (2019) A Review of Research on Adakites. *International Geology Review*, **63**, 47-64. https://doi.org/10.1080/00206814.2019.1702592

[47] Moyen, J. (2009) High Sr/Y and La/Yb Ratios: The Meaning of the "Adakitic Signature". *Lithos*, **112**, 556-574. https://doi.org/10.1016/j.lithos.2009.04.001

[48] Richards, J.P. and Kerrich, R. (2007) Special Paper: Adakite-Like Rocks: Their Diverse Origins and Questionable Role in Metallogenesis. *Economic Geology*, **102**, 537-576. https://doi.org/10.2113/gsecongeo.102.4.537

[49] Pilet, S., Baker, M.B. and Stolper, E.M. (2008) Metasomatized Lithosphere and the Origin of Alkaline Lavas. *Science*, **320**, 916-919. https://doi.org/10.1126/science.1156563

[50] Gómez-Frutos, D. and Castro, A. (2023) Mafic Microgranular Enclaves (MMEs) Trace the Origin of Post-Collisional Magmas. *Geology*, **51**, 743-747. https://doi.org/10.1130/g51248.1

[51] Christofides, G., Perugini, D., Koroneos, A., Soldatos, T., Poli, G., Eleftheriadis, G., *et al*. (2007) Interplay between Geochemistry and Magma Dynamics during Magma Interaction: An Example from the Sithonia Plutonic Complex (NE Greece). *Lithos*, **95**, 243-266. https://doi.org/10.1016/j.lithos.2006.07.015

[52] Perugini, D., Poli, G., Christofides, G. and Eleftheriadis, G. (2003) Magma Mixing in the Sithonia Plutonic Complex, Greece: Evidence from Mafic Microgranular Enclaves. *Mineralogy and Petrology*, **78**, 173-200. https://doi.org/10.1007/s00710-002-0225-0

[53] Vermeesch, P. (2006) Tectonic Discrimination Diagrams Revisited. *Geochemistry, Geophysics, Geosystems*, **7**, Q06017. https://doi.org/10.1029/2005gc001092

[54] Kilias, A. (2023) The Alpine Geological History of the Hellenides from the Triassic to the Present—Compression vs. Extension, a Dynamic Pair for Orogen Structural Configuration: A Synthesis. *Geosciences*, **14**, Article No. 10. https://doi.org/10.3390/geosciences14010010

[55] Kilias, A., Frisch, W., Avgerinas, A., Dunkl, I., Falalakis, G. and Gawlick, H.-J. (2010). Alpine Architecture and Kinematics of Deformation of the Northern Pelagonian Nappe Pile in the Hellenides. *Austrian Journal of Earth Sciences*, **103**, 4-28. https://doi.org/10.23689/fidgeo-2784

[56] Burg, J.-P. (2012) Rhodope: From Mesozoic Convergence to Cenozoic Extension. Review of Petro-Structural Data in the Geochronological Frame. *Journal of the Virtual Explorer*, **42**, 1-44. https://doi.org/10.3809/jvirtex.2011.00270

[57] Robertson, A.H.F., Trivić, B., Đerić, N. and Bucur, I.I. (2013) Tectonic Development of the Vardar Ocean and Its Margins: Evidence from the Republic of Macedonia and Greek Macedonia. *Tectonophysics*, **595**, 25-54. https://doi.org/10.1016/j.tecto.2012.07.022

[58] Scherreiks, R. and BouDagher-Fadel, M. (2021) The Closure of the Vardar Ocean (the Western Domain of the Northern Neotethys) from the Early Middle Jurassic to the Paleocene Time, Based on the Surface Geology of Eastern Pelagonia and the Vardar Zone, Biostratigraphy, and Seismic-Tomographic Images of the Mantle below the Central Hellenides. *UCL Open Environment*, **3**, Article No. 3. https://doi.org/10.14324/111.444/ucloe.000024

[59] Serafimovski, T., Boev, B. and Tasev, G. (2024) Post-Collision Magmatism and Metallogeny in the Southern Part of the Balkan Peninsula, SE-Europe (35th IGC abstract 83).